Radiological Imaging

The Theory of Image Formation, Detection, and Processing

Volume 1

Harrison H. Barrett
William Swindell

Department of Radiology
and
Optical Sciences Center
University of Arizona
Tucson, Arizona

1981

ACADEMIC PRESS
A Subsidiary of Harcourt Brace Jovanovich, Publishers

New York London
Paris San Diego San Francisco
São Paulo Sydney Tokyo Toronto

5.4 THE GAMMA-RAY CAMERA

5.4.1 General Description

The most commonly used gamma-ray camera is the instrument due to Anger *et al.* (1956; Anger, 1958, 1961). An image of a body organ is formed on a large scintillation crystal by means of a collimator, as described in Section 4.5, and the scintillations are viewed by an array of photomultipliers arranged on a close-packed hexagonal array. An analog computing circuit determines the location of the scintillation in the crystal and sends positioning signals to a display oscilloscope. With each scintillation event, the display brightness is momentarily turned up. This creates a flash of light on the display screen at a place that corresponds to the position of the scintillation within the crystal. The flashes are integrated on a photographic film, and over a period of time enough points are recorded to generate an image. In another method the coordinates of each flash are recorded using a minicomputer. The image is then displayed by recalling these coordinate values and displaying them on a cathode ray tube. In either case, if the count rate is sufficiently high "real-time" dynamic studies can be performed by generating a series of time-sequenced images.

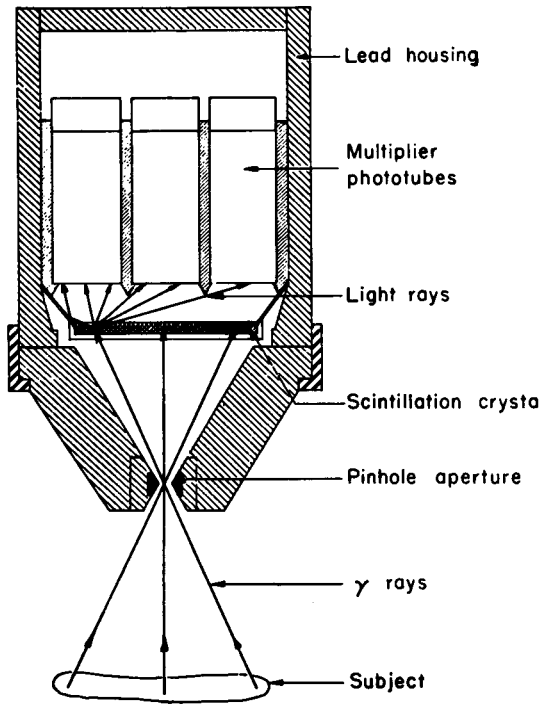

Fig. 5.39 Simplified diagram of an Anger camera employing seven photomultiplier tubes. A pinhole aperture forms a gamma-ray image of the subject on a sodium iodide scintillation screen. The position of each scintillation is determined by the phototube array and position computer, enabling the image to be relayed to and displayed on a CRT monitor. (From Anger, 1967.)

Figures 5.39 and 5.40 show a cross section of the camera head and a block diagram of the whole system for an Anger camera using seven phototubes.

The circuit that computes the position of each scintillation event works as follows. The output pulses from the phototubes are connected to four output wires with small capacitors. The center tube has equal coupling (20 pF) to all output wires, whereas the other tubes are connected by capacitors, the sizes of which are related to the position of the tube. For example, tube number 2, which is displaced from the center in the positive x direction, is connected to the x^+ output wire with a larger capacitor (40 pF). Tube number 3, being in the positive x, negative y quadrant, is coupled strongly (30 pF) to the x^+ wire, weakly (10 pF) to the x^- wire, strongly (40 pF) to the y^- wire, and not at all to the y^+ wire. As shown in the figure, the output wires are connected to difference circuits which drive the x and y inputs of the

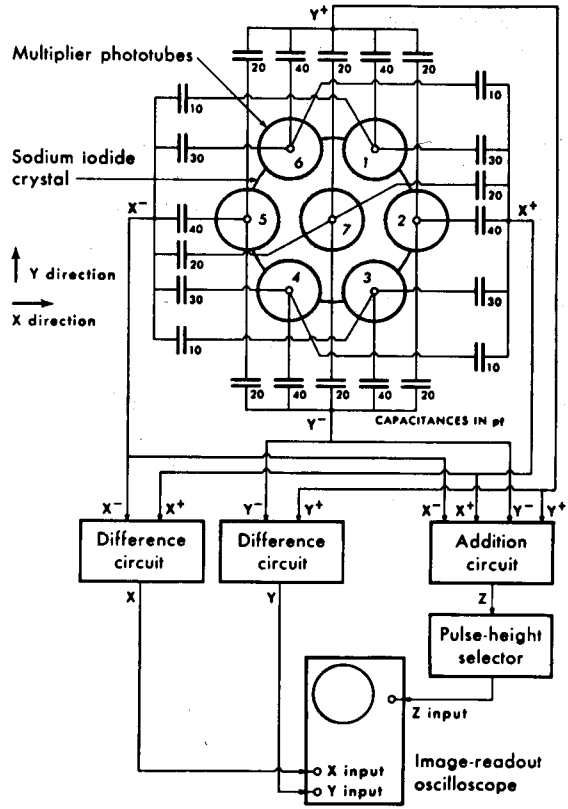

Fig. 5.40 Block diagram showing major components and principle of operation of a seven-tube scintillation camera. (From Anger, 1967.)

display CRT. Because of the proportional weighting of the phototube outputs to the x and y deflection voltages, the spot on the CRT will be deflected to a position that closely copies the site of the pertinent scintillation.

Consider a scintillation taking place under the center of phototube number 5. Most of the optical photons will be gathered by this tube. The other tubes will receive fewer photons in accordance with the decreasing solid angle subtended by them. The light will spread symmetrically in the plus and minus y directions, resulting in equal y^+ and y^- signals, and there will be no net deflection in the y direction of the CRT spot. However, tube number 5 will contribute a large signal to the x^- signal wire, driving the CRT spot to the left of the screen. Smaller x^+ and x^- signals will be generated by the other phototubes, and they will also contribute in determining the final position of the spot. The important point to notice is that the remapping of

the scintillation position onto the CRT face plate proceeds in a spatially continuous manner even though there are only seven nonimaging detectors in the system.

There is an additional circuit that sums all of the output signals and generates a pulse that is proportional to the optical energy in the flash. This pulse is used to gate the brightness modulation of the display. Pulses whose amplitude lies outside some preset limits are not included in the final image. The energy pulse is also used to improve display linearity. These topics will be expanded upon later.

The earliest system used only seven photomultipliers. Modern clinical systems, however, have at least two additional rings of tubes, giving an array total of 37 tubes or more. The largest current system has five concentric hexagonal arrays around the central tube for a grand total of 91 photodetectors.

Other types of medical gamma-ray cameras are surveyed in Moody *et al.* (1970) and McKeighen (1980).

5.4.2 Details of Operation

Position Arithmetic

We now show how the position of the scintillation is determined using the pulses that occur at the anodes of the phototube array. The method is most easily understood by considering a one-dimensional system. The extension to two dimensions is straightforward.

Consider the array of five tubes whose centers are located at $x = -2$, -1, 0, $+1$, and $+2$ as shown in Fig. 5.41. The height of the voltage pulse at the anode of the tube $V_i(x)$ depends on the position x of the scintillation event as shown in the lower part of the figure. Each $V_i(x)$ has a rounded profile centered on the axis of the tube. This idealized case neglects any edge effects caused by finite crystal size. The pulse from the ith tube is coupled to the output lines by the potential dividers formed by capacitor pairs (C_i^-, C^-) for the $V^-(x)$ line and (C_i^+, C^+) for the $V^+(i)$ line. In practice, we have $C^+ = C^- = C$, and C_i^+, $C_i^- \ll C$. Thus we have

$$V^+(x) = \sum_i V_i(x) w_i^+, \tag{5.181}$$

$$V^-(x) = \sum_i V_i(x) w_i^-, \tag{5.182}$$

where the relative weights $w_i^\pm$ are given by

$$w_i^\pm = C_i^\pm / C \tag{5.183}$$

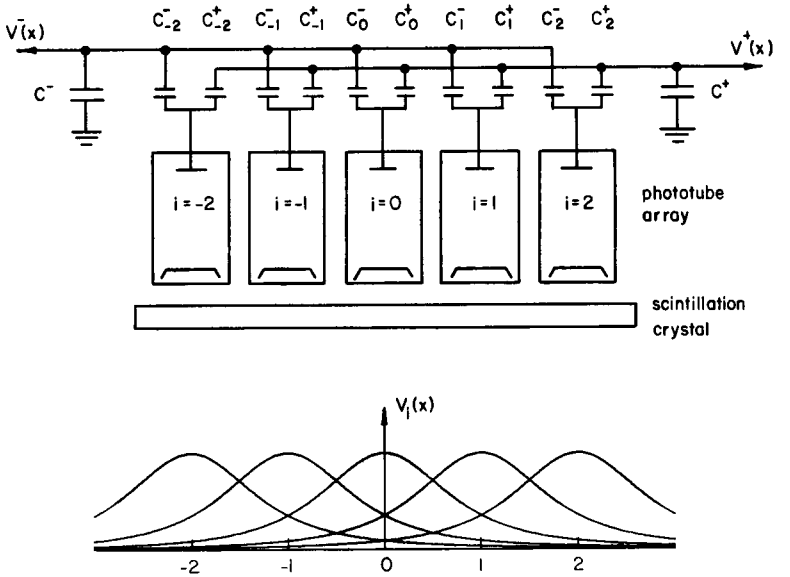

Fig. 5.41 Phototube outputs are coupled to the output lines by a voltage divider network made up of capacitors. Each tube has nominally the same response curve, $V_i(x)$, appropriately positioned, as shown in the lower part of the figure.

and are thus variable at the designer's choice. The two signals of interest are formed by adding and subtracting $V^+(x)$ and $V^-(x)$ to yield the position signal $V(x)$ and the energy signal $V^E(x)$:

$$V(x) = V^+(x) - V^-(x) = \sum_i V_i(x)(w_i^+ - w_i^-), \tag{5.184}$$

$$V^E(x) = V^+(x) + V^-(x) = \sum_i V_i(x)(w_i^+ + w_i^-). \tag{5.185}$$

The problem is to choose the weights $w_i^\pm$ and the individual tube responses such that $V(x)$ as given by (5.184) is linearly proportional to x. The response curve $V_i(x)$ is governed mainly by the geometry of the crystal and phototubes, but it is also influenced by reflection losses at the various interfaces and, in actual cameras, by a complicated light-baffle arrangement between the scintillator and the phototube array. Indeed, much of the proprietary aspect of Anger camera design is associated with the design of this optical element.

Returning to our one-dimensional example, we can see that the $w_i^\pm$ are particularly easy to determine for the case where $V^i(x)$ has the ideal triangular shape of width two units and centered at $x = x_i$. Figure 5.42 shows that an exactly linear response is obtained by making $w_i^\pm$ linearly dependent upon

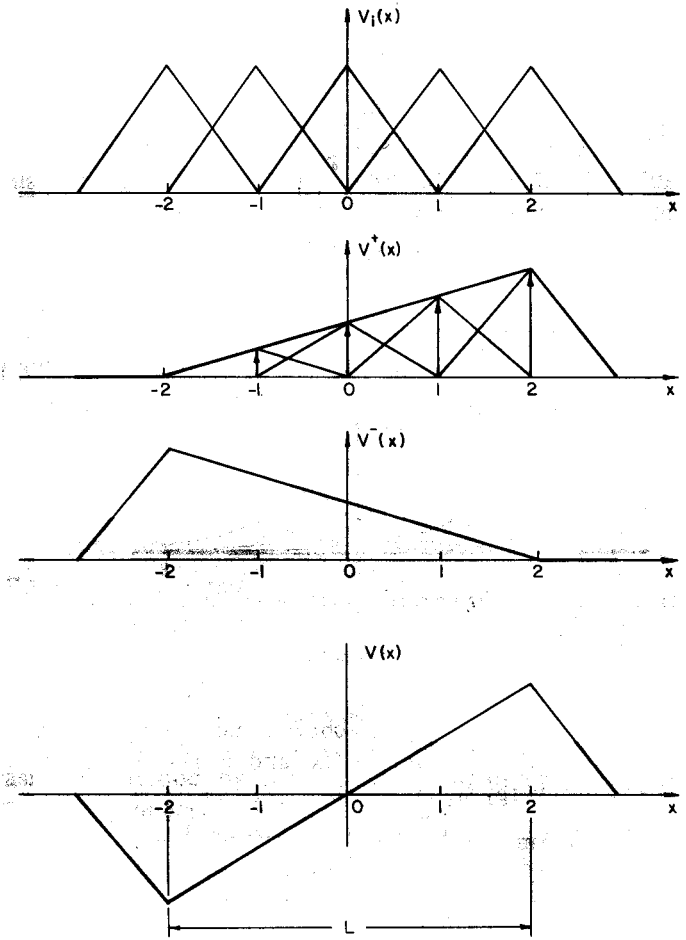

Fig. 5.42 For the idealized triangular response $V_i(x)$ shown at the top, $V^+(x)$ and $V^-(x)$ can be made triangular ramps by choosing the weights $w_i^{\pm}$, here depicted by vertical arrows, according to (5.186). The position signal $V(x) = V^+(x) - V^-(x)$ is exactly linear over the range $-L/2 < x < L/2$.

the x_i as follows:

$$w_i^+ \propto (\tfrac{1}{2}L + x_i),$$
$$w_i^- \propto (\tfrac{1}{2}L - x_i), \tag{5.186}$$

where L is the distance between the centers of the outer phototubes. In practice, the responses $V_i(x)$ are necessarily smoother than the triangle function, and the effect of the smoothing is shown in Fig. 5.43.

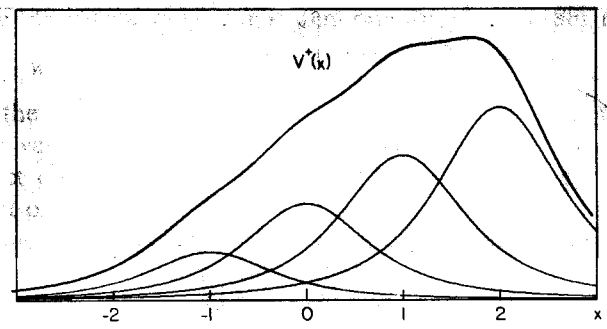

Fig. 5.43 For realizable forms of $V_i(x)$, the linearly weighted sum $V^+(x)$ is no longer linear with x.

We now demonstrate some important design considerations by means of a simple numerical example. For this example, we assume that the $V_i(x)$ curves are determined by the solid angle $\Omega_i(x)$ subtended by the ith detector for a scintillation located at point x as shown in Fig. 5.44. Provided that the height d of the detector array above the crystal is not too small, we can approximate $V_i(x)$ as follows:

$$V_i(x) \propto \Omega_i(x) \propto \cos^3 \theta, \tag{5.187}$$

where θ is defined in Fig. 5.44.

For this example, we choose $d = 1$. Then $V_i(x)$ is given by

$$V_i(x) \propto [1 + (x_i - x)^2]^{-3/2}. \tag{5.188}$$

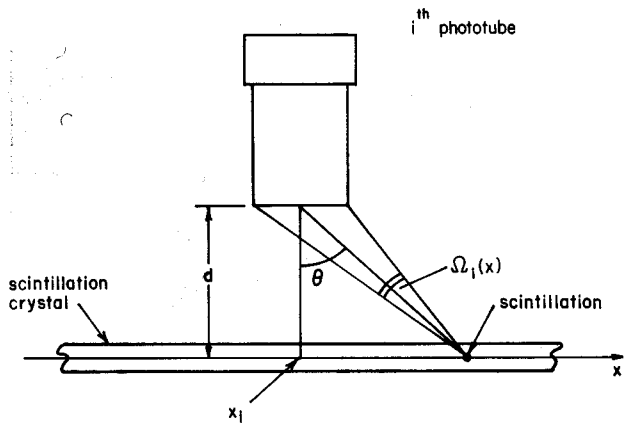

Fig. 5.44 Geometry showing solid angle $\Omega_i(x)$ subtended by ith phototube from scintillation located at x.

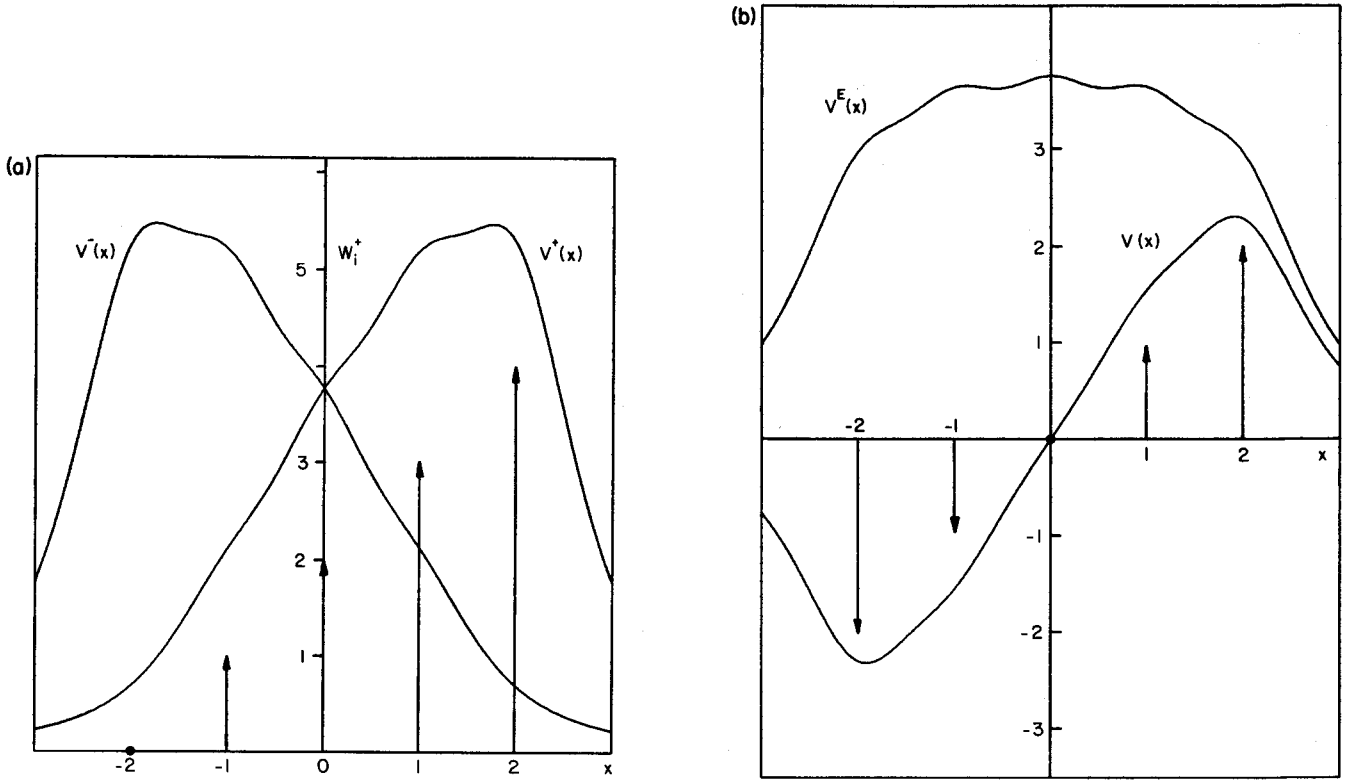

Fig. 5.45 (a) Positive and negative output signals using linear weights in a theoretical one-dimensional camera system. The positive signal weights w_i^+ are depicted by arrows. The negative weights w_i^- are not shown but are symmetrical to the w_i^+ and given by $w_i^- = 4 - w_i^+$. (b) The corresponding position signal $V(x)$ is approximately proportional to x over most of the aperture of the array. The energy signal $V^E(x)$, which should be independent of x, varies considerably over this same range. Total weight, $w_i = w_i^+ - w_i^-$, is also shown by arrows.

When we use the linear weighting system prescribed by (5.186), namely

$$w_i^+ = i + 2, \qquad w_i^- = 2 - i, \qquad (i = 0, \pm 1, \pm 2), \tag{5.189}$$

we obtain the results shown in Fig. 5.45. It is apparent that the position signal is not very linear over the full extent of the array, and even though we have not yet discussed the desirability of having the energy signal $V^E(x)$ independent of x, it is clear that with this weighting scheme this condition is not well met over the aperture of the camera. It is found empirically that by increasing the weights associated with the end detectors in the array, both of these defects can be somewhat remedied. For example, simply by increasing the largest weights w_2^+ and w_{-2}^- from 4.0 to 5.5, both the linearity of the $V(x)$ signal and the constancy of the $V^E(x)$ signal are improved. This is shown in Fig. 5.46.

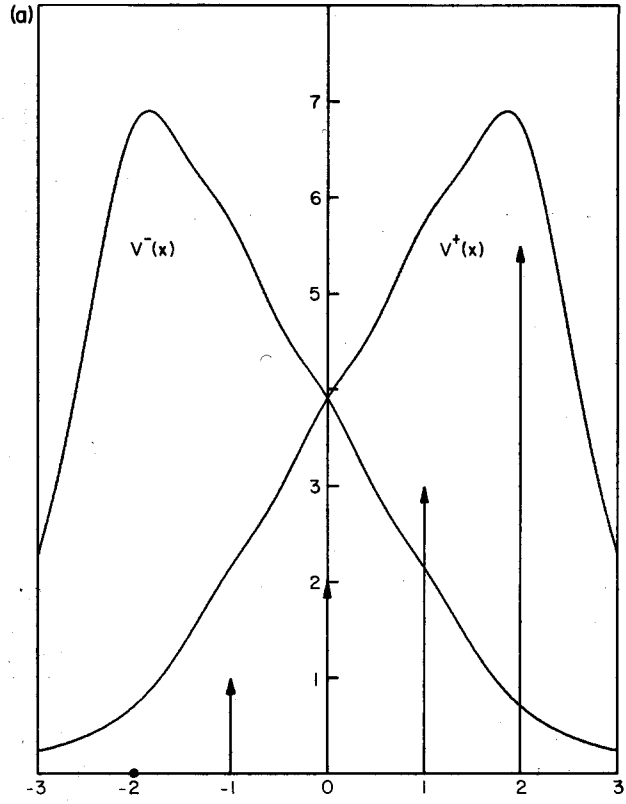

Fig. 5.46 The same variables as in Fig. 5.45 but with the outer weights w_2^+ and w_{-2}^- increased from 4.0 to 5.5. In (b) (on next page) it is seen that the position signal is more linear over a wider range and the energy signal is more nearly constant over the array aperture.

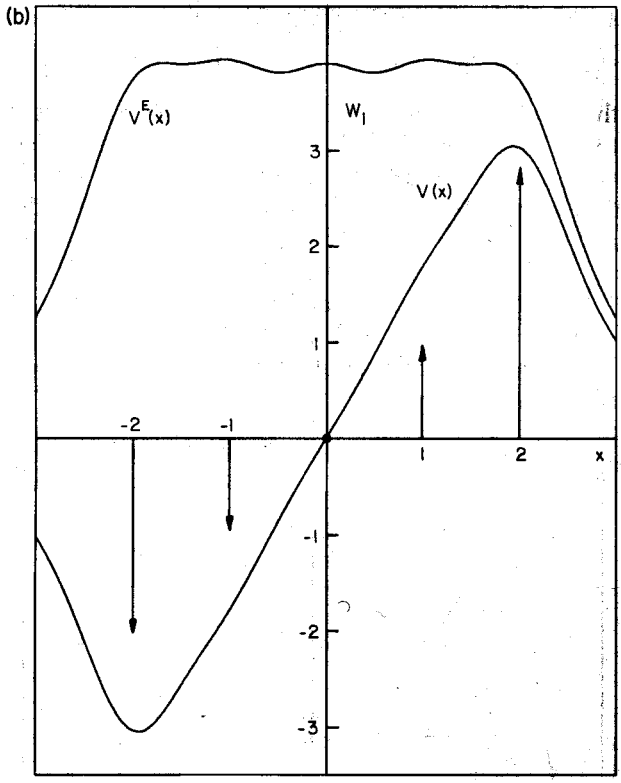

Fig. 5.46 *(continued)*

The foregoing results, even though based on a simple one-dimensional situation, are qualitatively applicable to real two-dimensional cameras. The weighting factors associated with each tube in a two-dimensional camera array are, except for the outermost tubes, linearly related to the (x, y) coordinates of the tube axis. It is again desirable to overemphasize the contribution from the outermost tubes.

The Energy Signal

We have so far assumed that all optical flashes on the scintillator are equally intense. In fact, the optical flashes have a range of energies, and this will affect the final image quality if compensatory steps are not taken. First, we consider the optical pulse-height spectrum for monoenergetic incident gamma rays. A typical spectrum is shown in Fig. 5.47. There are two main

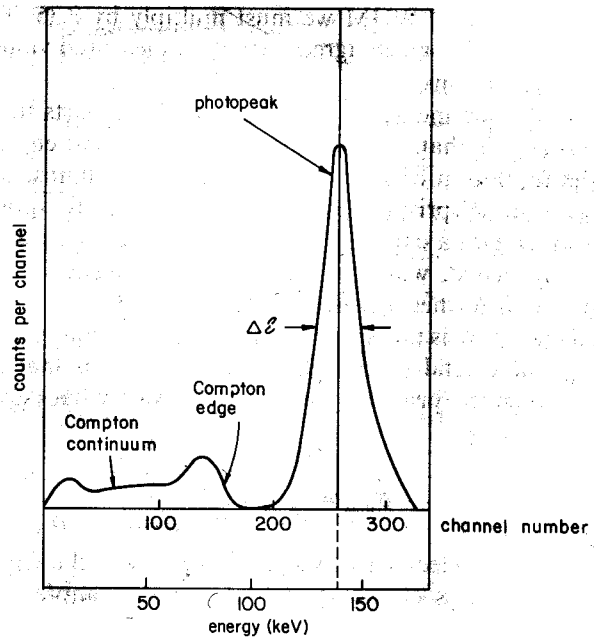

Fig. 5.47 Optical pulse height spectrum for typical NaI crystal and 140-keV gamma rays. The photopeak is derived from total-absorption events only, whereas single Compton scattering events in the crystal, which account for most of the low-energy part of the distribution, can contribute only below the Compton edge at 90.4 keV. Compton scattering in the patient's body, on the other hand, contributes strongly in the range 100–140 keV.

features, namely the photopeak and the Compton continuum. The photopeak corresponds to events in which the whole energy of the incident gamma ray is released in the crystal. This may be a photoelectric absorption or a Compton scattering process followed by a photoelectric absorption. These processes are described in Appendix C.

One important feature of the photopeak is its energy resolution, which is generally stated as the full width of the peak at half of its maximum height (FWHM). The FWHM can be estimated with reasonable accuracy by applying Poisson statistics to the number of detected optical photons contributing to the photopeak. For example, consider gamma rays of energy 140 keV (from ^{99m}Tc) striking a NaI scintillator. It takes approximately 30 eV to produce each optical photon, and about half of these will strike the photocathode in a well-designed scintillation detector. If we assume a quantum efficiency of 25% at the photocathode, the mean number of detected photons will be $14 \times 10^4 \times 0.25 \times 0.50/30 \approx 580$. The normalized standard deviation of this quantity according to Poisson statistics is $1/\sqrt{580} = 4.2\%$, and to

convert to a normalized FWHM we must multiply by 2.35. This yields a theoretical $\Delta\mathscr{E}/\mathscr{E}$ of 9.7%, which agrees well with measured values obtained under favorable conditions.

An additional experimental observation which supports the hypothesis of Poisson statistics is that, over a wide range of incident energies $\mathscr{E}_\gamma$, it is found that the resolution of the photopeak improves almost linearly with $(\mathscr{E}_\gamma)^{1/2}$. It may seem surprising that Poisson statistics are applicable since we are not dealing with a counting experiment where the source events are completely uncorrelated, which is the usual prerequisite for the Poisson result. The subject is further discussed in Section 5.5.3.

If the total energy $\mathscr{E}_\gamma$ is not absorbed, then the maximum energy that can be imparted to the crystal in a single Compton event is that given to the recoil electron when the primary gamma ray is exactly backscattered. This energy $\mathscr{E}_{\max}$ is given by

$$\mathscr{E}_{\max} = \frac{\mathscr{E}_\gamma^2}{\mathscr{E}_\gamma + 255}, \tag{5.190}$$

(for $\mathscr{E}_\gamma$ in units of kilo-electron-volts) and is known as the Compton edge. For gamma ray energies of less than 1 meV, the Compton edge is well separated from the photopeak, which accounts for the trough immediately below the photopeak in the pulse height spectrum. Multiple Compton events tend to fill in the trough to some extent. At higher energies, more overlap occurs between the photopeak and Compton edge.

There are other mechanisms that contribute to low-energy counts, but they are of little interest to this discussion.

When considering the effect that the optical pulse-height spectrum (OPHS) has on the final image produced by an Anger camera, it must be realized that only photopeak events can be accepted as part of the imaging data. While it is true that many low-energy events are caused by bona fide imaging photons undergoing a Compton interaction in the detector, it is also true that many low-energy optical pulses are caused by gamma rays that lost energy by scattering first in the patient's body. Scattered rays contain essentially no useful imaging information and serve only to degrade the image contrast by adding a background fog level.

The position computer described in the previous section is sensitive to fluctuations within the photopeak. The indicated position coordinate will be directly proportional to the total optical energy detected [see (5.184)]. It is customary to use high-speed dividers, as shown in Fig. 5.48, which divide the position signals by the energy signal. This considerably reduces the fluctuations in image display coordinates that arise from fluctuations in the optical pulse.

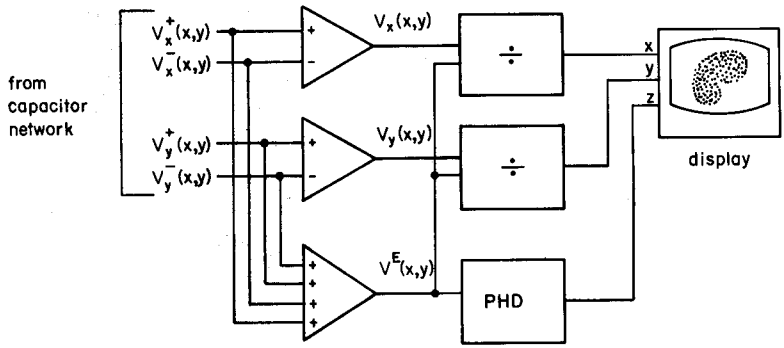

Fig. 5.48 Energy signal $V^E(x, y)$ is used to normalize the position signals $V_x(x, y)$ and $V_y(x, y)$ by means of the divider circuits. In addition, it drives a pulse-height discriminator (PHD) that controls the display brightness. Normally only photopeak events are displayed.

5.4.3 Spatial Resolution

In Section 4.5 we studied the spatial resolution of the Anger camera as determined by the collimator geometry. Now we study the intrinsic resolution of the camera itself. Consider a situation in which a perfectly collimated, infinitesimally narrow beam of gamma rays impinges upon a given point of the scintillation crystal. The corresponding flashes on the output display will not form an equally precise spot. There will be a spread that is caused in part by statistical fluctuation in the optical photon fluxes reaching the phototubes and in part by the random direction associated with the Compton recoil electron in the crystal.

Photon Statistics

We are interested in the statistical fluctuations that occur in the voltage pulse at the anode of each phototube. Earlier we argued that Poisson statistics apply when determining the fluctuations in the total number of optical photons created by monoenergetic gamma rays undergoing a photopeak interaction. The fluctuations in the number of optical photons reaching any one photocathode will also be Poisson distributed since we have the original Poisson distribution serving as input to a binomial process which, as shown in Section 3.4.4, leaves a Poisson distribution. The binomial probability is simply the probability that an optical photon will reach the photocathode in question. It depends mainly upon the solid angle subtended by that photocathode from the source of scintillation. There is yet another binomial

process, namely, that of generating photoelectrons in the phototube. The probability of this event is simply the quantum efficiency of the photocathode. The result, of course, is that the number of photoelectrons in the tube also has a Poisson distribution. At this point we assume that the electron multiplication process in the tube adds no additional noise to the system and that the fluctuations of the output voltage pulse are a direct copy of the fluctuations in the photoelectron stream leaving the photocathode. We incur a slight error for neglecting the (largely unknown) statistical properties of the secondary multiplication process (see Section 5.5.2).

Following Tanaka *et al.* (1970), we write

$$\mathbf{V}_i = G\mathbf{n}_i, \tag{5.191}$$

where $\mathbf{V}_i$ is the height of the voltage pulse appearing at the output of the ith phototube, $\mathbf{n}_i$ is the number of photoelectrons departing from the photocathode, and G is a gain factor with appropriate dimensionality. Again we consider only the x direction in this analysis; the analysis for the y direction is identical.

The x-axis deflection voltage, now treated as a random variable, is given by (5.184):

$$\mathbf{V}(x) = \sum \mathbf{V}_i w_i, \tag{5.192}$$

where we have replaced $(w_i^+ - w_i^-)$ by w_i.

It is straightforward to determine the variance of the deflection-voltage fluctuations:

$$\Delta\mathbf{V}(x) = \mathbf{V}(x) - \bar{V}(x) = \sum_i \Delta\mathbf{V}_i w_i = G \sum_i w_i \Delta\mathbf{n}_i, \tag{5.193}$$

$$\sigma_{\Delta V}^2 = \langle \Delta\mathbf{V}^2 \rangle = G^2 \left\langle \sum_i w_i \Delta\mathbf{n}_i \sum_j w_j \Delta\mathbf{n}_j \right\rangle. \tag{5.194}$$

From (3.181), we know that

$$\langle \Delta\mathbf{n}_i \Delta\mathbf{n}_j \rangle = 0 \qquad \text{if} \quad i \neq j. \tag{5.195}$$

Thus we can write

$$\sigma_{\Delta V}^2 = G^2 \left\langle \sum_i w_i^2 \Delta\mathbf{n}_i^2 \right\rangle, \tag{5.196}$$

which, because of the Poisson statistics, can be written

$$\sigma_{\Delta V}^2 = G^2 \sum_i w_i^2 \bar{n}_i. \tag{5.197}$$

To convert the standard deviation of the deflection voltage $\sigma_{\Delta V}$ to a spatial standard deviation σ_x, we must divide by the mean voltage sensitivity

gradient S:

$$\sigma_x = \sigma_{\Delta V}/S, \tag{5.198}$$

where

$$S = \frac{d\bar{V}(x)}{dx} = G\sum_i w_i \frac{d\bar{n}_i}{dx}. \tag{5.199}$$

Note that the FWHM of the PSF δ is related to σ_x by $\delta = 2.35\sigma_x$ if we assume that the PSF is Gaussian.

Combining (5.197) and (5.199), we obtain

$$\sigma_x = \left(\sum_i w_i^2 \bar{n}_i\right)^{1/2} \Big/ \left(\sum_i w_i \frac{d\bar{n}_i}{dx}\right). \tag{5.200}$$

This is the fundamental equation that determines the spatial resolution of the system in terms of the phototube weights and the individual-tube spatial response functions.

We are seeking the optimum weights that will minimize the value of σ_x, so we proceed by forming the partial derivative $\partial\sigma_x/\partial w_j$:

$$\frac{\partial\sigma_x}{\partial w_j} = \frac{\left(\sum_i w_i^2 \bar{n}_i\right)^{-1/2} w_j \bar{n}_j}{\sum_i w_i \, d\bar{n}_i/dx} - \frac{\left(\sum_i w_i^2 \bar{n}_i\right)^{1/2} d\bar{n}_j/dx}{\left(\sum_i w_i \, d\bar{n}_i/dx\right)^2}. \tag{5.201}$$

By setting this result to zero, we find the conditions for which w_j is the optimum weight for the jth phototube when all other tubes, $(i \neq j)$, are not necessarily optimally weighted. Calling this quantity $w_j'(\text{opt})$ we find that

$$w_j'(\text{opt}) = \frac{1}{\bar{n}_j}\frac{d\bar{n}_j}{dx}\left(\sum_i w_i^2 \bar{n}_i\right) \Big/ \left(\sum_i w_i \, d\bar{n}_i/dx\right). \tag{5.202}$$

The fully optimized w_j is found by requiring that the w_i are also the optimum values. Therefore, we can write the solution for fully optimal weights $w_j(\text{opt})$ in the implicit manner,

$$w_j(\text{opt}) = \frac{1}{\bar{n}_j}\frac{d\bar{n}_j}{dx}\left(\sum_i w_i^2(\text{opt})\bar{n}_i\right) \Big/ \left(\sum_i w_i(\text{opt})\, dn_i/dx\right). \tag{5.203}$$

By inspection, it is seen that one nontrivial solution to this set of nonlinear simultaneous equations is

$$w_j(\text{opt}) = k\frac{1}{\bar{n}_j}\frac{d\bar{n}_j}{dx}, \tag{5.204}$$

where k is an undetermined constant. Note that the optimum weight for a given (jth) tube depends only on its own response curve $\bar{n}_j$ and not on the other responses $\bar{n}_i$, $i \neq j$. The minimum resolution distance is now given by substituting (5.204) into (5.200):

$$\sigma_{x,\min} = \left[\sum_i \frac{1}{\bar{n}_i}\left(\frac{d\bar{n}_i}{dx}\right)^2\right]^{-1/2} \tag{5.205}$$

We illustrate the use of these equations with a simple example. The geometry is shown in Fig. 5.44. We assume that optical photons are emitted isotropically from the scintillation point, and we neglect reflection, refraction, and absorption effects. If the mean number of photons emitted per scintillation is $\bar{N}$, the mean number of photoelectrons in the jth tube $\bar{n}_j$ is

$$\bar{n}_j/\bar{N} = \eta\Omega_j(x)/4\pi, \tag{5.206}$$

where η is the quantum efficiency of the photocathode, and $\Omega_j(x)$, the solid angle subtended by the photocathode, is given by

$$\Omega_j(x) \approx A\cos\theta/l^2. \tag{5.207}$$

Thus

$$\Omega_j(x) = \frac{Ad}{[(x - x_j)^2 + d^2]^{3/2}}, \tag{5.208}$$

where d is the height of the photocathode, x is the position of the scintillation event, and x_j is the position of the jth photodetector.

Using (5.204), (5.206), and (5.208), we obtain

$$w_j(\text{opt}) = \frac{2k(x - x_j)}{(x - x_j)^2 + d^2}. \tag{5.209}$$

Figure 5.49 shows the functional form of $w_j(\text{opt})$. It is seen that the optimum weight is strongly position dependent, but depends only on the distance to the scintillation $(x - x_j)$. To provide the minimum resolving distance, the optimum weights must be changed for each event according to the location of the event.

The Anger camera has fixed weights determined by the capacitor networks. As a basis for comparison with the ideal system, we choose the fixed weights according to (5.209) for $x = 0$. This will permit $\sigma_{x,\min}$ to be realized for events occurring at the center of the camera. The fixed weights for this five-tube (one-dimensional) camera are shown by the arrows in Fig. 5.49. There is clearly a conflict between the weighting requirements that optimize the resolution (even at a single point) and those that provide the best linearity as illustrated in Fig. 5.46(b). This is a fundamental problem with fixed weight-

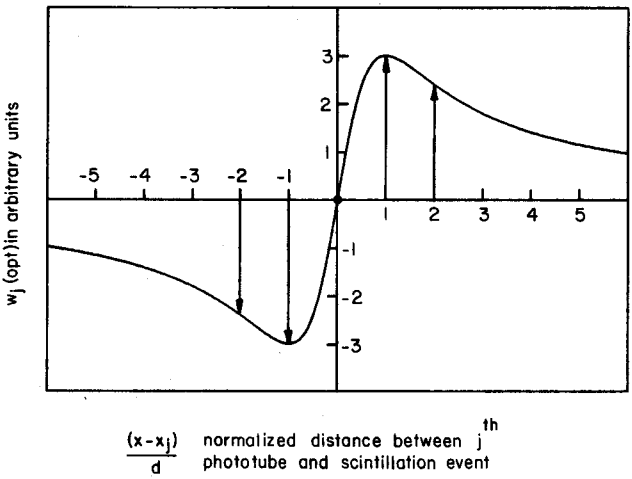

Fig. 5.49 Solid curve shows the optimum weighting factor for the jth tube located at x_j for a scintillation event positioned at x. For comparison with the fixed weights of the Anger camera, arrows show the set of fixed weights that would be used for an array of five tubes with uniform inter-tube separation equal to the height d of the tube above the crystal.

ing systems. We shall see shortly that position-dependent (or *floating*) weights can be achieved using delay lines.

Qualitatively, we can understand the shape of the curve in Fig. 5.49 by referring to Fig. 5.50. The relative importance of a signal from the jth phototube is directly related to the amount of positional information that it contains. The positional uncertainty Δx_A associated with a photoelectron pulse of height n_A is determined primarily by the slope $d\bar{n}_j/dx$ evaluated at x_A. Note that the event could be at either location shown as $\pm x_A$ in Fig. 5.50 and that the ambiguity is resolved when signals from the other phototubes are also considered. Weak pulses of height n_B from distant events are associated with a larger position uncertainty, primarily because of the reduced slope at that point. In the optimum weighting system these pulses are weighted less. Notice also that a very strong pulse located on the tube axis receives no weight at all. In a differential sense, it contributes no information regarding the position of the event, i.e., $d\bar{n}_j/dx = 0$ at $x - x_j = 0$.

We close the analysis of this simple one-dimensional model by determining $\sigma_{x,\min}$, using (5.205), (5.206), and (5.208) for the case $d = 1$, $\eta = 20\%$, and $\bar{N} = 5000$. The result is shown in Fig. 5.51. Over the central part of the array, the minimum resolution distance stays fairly constant with a normalized rms fluctuation of about 6%. The resolution is poorer when the event is located exactly under a phototube as explained in the previous paragraph, and degrades with extreme rapidity outside the aperture of the camera.

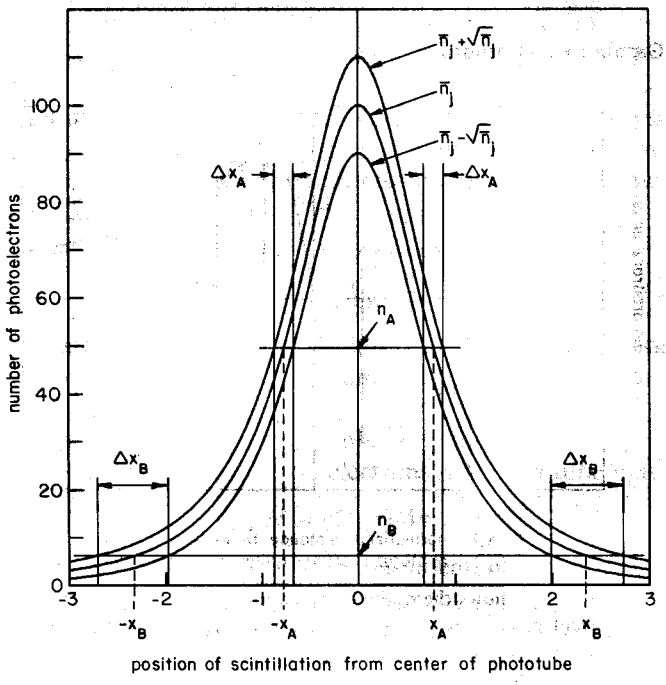

Fig. 5.50 Average number of photoelectrons generated in a phototube is shown (central curve) plotted as a function of the distance to the scintillation point for a typical Anger camera geometry. The outer curves represent one standard deviation from this value. The positional uncertainty associated with distant scintillations, Δx_B is greater than that for nearer ones Δx_A.

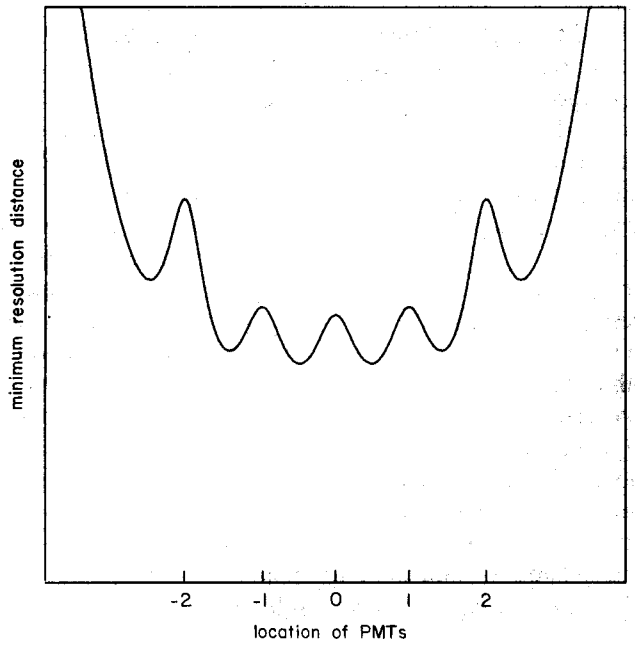

Fig. 5.51 Minimum resolution for one-dimensional camera using optimized weights. See text for details. At the mid point of the central tube the minimum resolution distance is 0.16 of the intertube separation.

We now show that the statistical fluctuations in the photon distribution really do affect the resolution on a scale that is important for clinical diagnosis. We must remember, however, that the total system resolution is greater than that predicted by $\sigma_{x,\min}(\text{opt})$ because of additional blurring due to collimator resolution (Section 4.5), scattered radiation (Chapter 11), and crystal thickness effects. We consider an array consisting of a central phototube surrounded by three rings of closely packed tubes as shown in Fig. 5.52. For this two-dimensional array, we must generalize (5.206) and (5.208) as follows:

$$\bar{n}_j = \frac{n\bar{N}}{4\pi} \frac{Ad}{[(x - x_j)^2 + (y - y_j)^2 + d^2]^{3/2}}. \tag{5.210}$$

The resolution $\sigma_{x,\min}(\text{opt})$ is a slowly varying function of x and y, so it is convenient to compute its value at $x = y = 0$, the center of the camera. Using (5.205) and (5.210), we now obtain

$$\sigma_{x,\min}(\text{opt}) = \left[\frac{9\bar{N}\eta Ad}{4\pi} \sum_j \frac{x_j^2}{(x_j^2 + y_j^2 + d^2)^{7/2}}\right]^{-1/2}, \tag{5.211}$$

where x_j, y_j are the coordinates of the jth phototube.

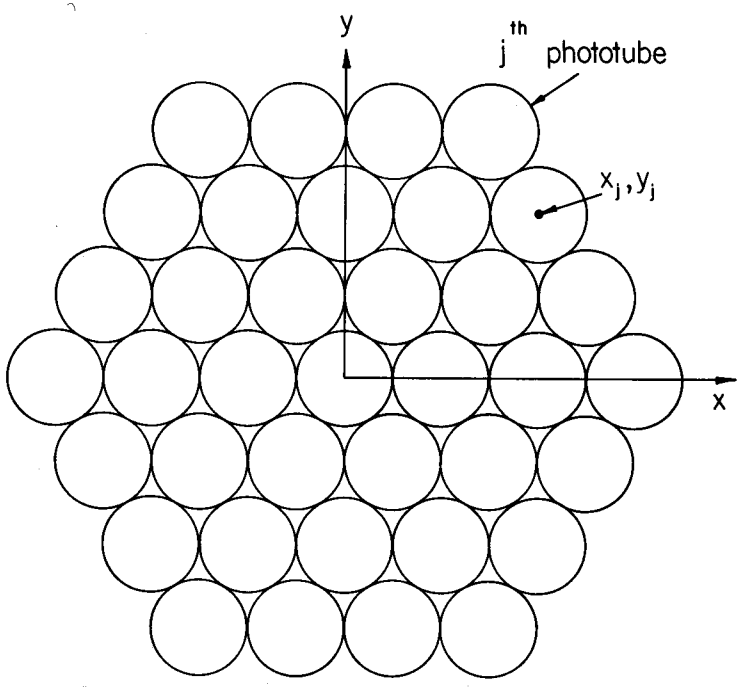

Fig. 5.52 Phototube arrangement for an array of 37 tubes in a close-packed array.

Using the typical values $d = 3.5$ cm, $A = 19.6$ cm^2 (a circular photocathode of diameter 5 cm), $\bar{N} = 5000$, $\eta = 0.2$, and assuming that the tubes are close packed with an intertube spacing of 5 cm, we find that

$$\sigma_{x,\min}(\text{opt}) = 0.257 \quad \text{cm}. \tag{5.212}$$

This is equivalent to a FWHM of the PSF given by

$$\delta = 2.35\sigma_{x,\min}(\text{opt}) = 0.60 \quad \text{cm}. \tag{5.213}$$

Next we examine the importance of the contributions from the outer rings. By summing over just the first ring, the first and second rings, and all three rings, we find that

$$\sigma_{x,\min}(\text{opt}) = \begin{cases} 0.294 & \text{cm} \quad (\text{ring 1}) \\ 0.263 & \text{cm} \quad (\text{rings 1 and 2}) \\ 0.257 & \text{cm} \quad (\text{rings 1, 2, and 3}). \end{cases} \tag{5.214}$$

We observe that essentially all of the positional information is derived from the nearest neighboring tubes in ring 1.

The number of resolvable spots per tube diameter, Q, is independent of the size of the phototube. Provided that all dimensions are scaled linearly, this result holds for any size system. This reflects a basic trade-off between the intrinsic camera minimum resolution distance, the number of phototubes, and the field of view of the camera. For a camera with N_T phototubes spanning a field of view of diameter D, the number of separately resolvable points along the diameter, n_{pixel}, is

$$n_{\text{pixel}} \approx N_T Q \tag{5.215}$$

and the intrinsic linear resolution will be

$$\delta \approx D/QN_T. \tag{5.216}$$

The only way to significantly improve the value of Q and camera performance is by increasing either the efficiency of the scintillation and hence $\bar{N}$, or the quantum efficiency of the photocathode. At the present time, there seems little hope for significantly improving either of these quantities. Thus the quest for decreasing the minimum resolvable distance will best be carried out by having a very large number of relatively small phototubes.

5.4.4 Threshold Preamplifiers

We have just seen that the weak signals from distant detectors should be weighted less strongly than stronger ones from near detectors. One way of

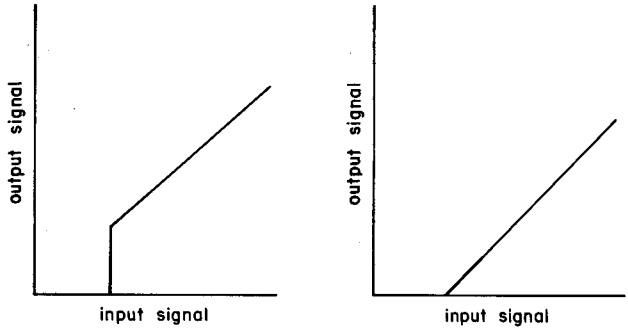

Fig. 5.53 Threshold preamplifiers with either of the above characteristics allow weak signals to be automatically rejected and not contribute to the position-determining analog computation.

automatically achieving this is to use threshold preamplifiers with each detector. The nonlinear characteristic of these amplifiers, shown in Fig. 5.53, results in weak signals being completely rejected. The advantage of the system is that the variable weights, in this case zero, move with the location of the scintillation and hence resemble in some sense the completely position-dependent weights prescribed by (5.204). This method (Kulberg and van Dijk, 1972) improves the spatial resolution of an Anger camera by about 15%.